small structures
www.small-structures.com

Micro-/Nanohierarchical Surfaces for Enhanced Pool Boiling in Large-Area Silicon Multichips

*Youngseob Lee, Kiwan Kim, Yunseo Kim, Daeyoung Kong, Jeonghwan Park, Daehyuk Son, Sungchan Kang, Seogwoo Hong, and Hyoungsoon Lee**

With the rising demand for data centers, the need for an efficient thermal management approach becomes increasingly critical. This study examines the enhancement in pool boiling heat transfer on a customized multichip module, designed to mimic artificial intelligence chip layouts for high-performance computing. Experiments are conducted on smooth surfaces and hierarchical structures integrating micropillars and porous copper, specifically copper inverse opal (CuIO) and copper nanowire (NW). The results demonstrate significant enhancements in critical heat flux (CHF) and heat transfer coefficient (HTC) through these hierarchical structures. Notably, the NW-CuIO-integrated hierarchical structure exhibits the highest CHF (234 W cm^{-2}), achieving a 166% enhancement over smooth silicon. The HTC enhancement is more pronounced for the CuIO-integrated hierarchical structure; this structure achieves an HTC of 70.3 kW m^{-2} K^{-1}, which represents a 166% improvement. The heater layout, engineered surfaces, and their synergistic effects are analyzed through visualization. The observed boiling inversion phenomena further underscore the importance of sequential activation of nucleation sites in improving boiling performance. This study provides valuable insights into the mechanisms governing the enhancement of boiling heat transfer and offers practical guidance for developing efficient thermal management solutions for data centers.

1. Introduction

The growing attention to machine learning, artificial intelligence (AI), cryptocurrencies, blockchain, cloud computing, and other data-intensive technologies is driving an unprecedented rise in demand for hyperscale data centers.[1,2] The global number of active hyperscale facilities has expanded significantly, and this growth is projected to continue over the next decade. The recent advent of generative AI models is expected to further accelerate energy consumption in data centers, beyond earlier predictions.[3,4] This increased energy demand necessitates careful management of the extreme heat dissipation during practical operation.[5,6]

In data centers, cooling accounts for 38% of the overall energy consumption, representing the second-largest energy consumption component after computing equipment, which uses ≈50% of the total power.[7,8] Despite this, most data centers continue to rely on air-based cooling systems, which are insufficient to meet the growing cooling demands of advanced AI superchips.[9] This inefficiency arises from the high thermal resistance between the chips and the ambient environment due to the relatively low convective heat transfer coefficient (HTC) associated with air cooling.[10] Furthermore, with the increasing demand for high-performance computing, chip manufacturing has reached a fundamental limit in scaling down transistor sizes. Consequently, processor power, thermal design power, and die sizes are expected to increase, leading to higher power densities in data centers.[11] Since cooling already accounts for a significant portion of data center energy consumption, these trends emphasize the need for more efficient cooling solutions. Thus, the development of innovative and energy-efficient cooling technologies is essential for maintaining the economic viability and reliability of data centers.

Liquid cooling offers significantly better performance than air cooling due to the superior thermophysical properties of commonly used refrigerants. In particular, phase-change cooling,

Y. Lee, K. Kim, J. Park, H. Lee
Department of Intelligent Energy and Industry
Chung-Ang University
Seoul 06974, South Korea
E-mail: leeh@cau.ac.kr

The ORCID identification number(s) for the author(s) of this article can be found under https://doi.org/10.1002/sstr.202400512.

DOI: 10.1002/sstr.202400512

Y. Kim, H. Lee
Department of Mechanical Engineering
Chung-Ang University
Seoul 06974, South Korea

D. Kong
Department of Mechanical Engineering
Stanford University
Stanford CA 94305, USA

D. Son, S. Kang, S. Hong
Device Research Center
Samsung Advanced Institute of Technology
Gyeonggi-Do 16677, South Korea

which utilizes latent heat, greatly reduces the thermal resistance between the chip and the ambient environment. This enables data centers to operate without relying on air-conditioning, the least energy-efficient component in the entire cooling system, thereby greatly enhancing the power usage effectiveness.[12–14] Several phase-change heat transfer methods for cooling have been studied, such as microchannels,[15] jet impingement,[16] and spray cooling.[17] While these methods are thermally effective, they require additional pumping power, which contradicts the requirement for minimizing power consumption. In contrast, some passive cooling systems, such as heat pipes[18] and thermosyphons,[19] are more energy-efficient in regard to input; however, their conventional heat transfer performance is inadequate for cooling high-performance data centers. Therefore, pool boiling has been highlighted as an alternative thermal management strategy.

Researchers have extensively investigated pool boiling heat transfer across various morphologies, emphasizing the relationship between bubble dynamics, thermal performance, and surface features.[20,21] For example, macro-, micro-, and nanostructural surface fabrications contribute significantly to the enhancement of critical heat flux (CHF) and HTC.[22] To enhance CHF, surface modifications are essential for ensuring a continuous supply of liquid, preventing dry-out from progressing to irreversible levels.[23] The most widely employed method in this regard is increasing hydrophilicity.[24] Hydrophilic surfaces facilitate horizontal liquid replenishment, which can mitigate the obstruction of liquid supply by vigorous bubble ebullition.[25] This effect is maximized on microstructured and hierarchically structured superhydrophilic surfaces, resulting in correspondingly higher CHF.[26–28] Alternatively, it also improves CHF by maintaining a liquid supply path, thereby minimizing the disruption in liquid transport during the bubble detachment process. This method is implemented in various manners, including nonheating area control[29] and adjustment of heterogeneous wettability[30–32] and, beyond these surface modifications, approaches such as a simple vapor shroud[33] or a permeable vapor wall.[34,35] Additionally, some researchers have analytically demonstrated how cavities trap gas and facilitate nucleation.[36,37] Since the entrapped gas promotes phase-change heat transfer by acting as a trigger for nucleation,[22] the ability to trap gas directly influences HTC. Further studies have reported substantial HTC enhancement based on this effect.[38,39] Moreover, re-entrant structures with tapered necks can be employed to capture gas more effectively.[40] In addition to these surface modifications, HTC enhancements can be achieved using approaches similar to certain methods for improving CHF, such as incorporating surfactants or applying electric fields to facilitate bubble detachment.[41,42] As mentioned earlier, numerous experiments have been conducted to study the thermal performance of pool boiling heat transfer.

Most previous studies have primarily focused on small heater sizes, typically less than 1 cm^2, with a single heat source; however, this does not accurately reflect the chip designs used in modern data centers. AI chips now feature significantly larger dies, reaching up to ≈800 mm^2, limited by reticle constraints.[11,43] With the advent of wafer-scale AI chips, these sizes are expected to increase further, which would complicate thermal management as cooling performance deteriorates with increasing size.[44] Additionally, these chips incorporate multiple distinct heat sources because of the heterogeneous integration necessary for enhancing performance, power efficiency, and flexibility in design and functionality.[45] This can lead to significant deviations in thermal performance from previously reported findings when such chips are utilized in data centers since boiling performance and bubble dynamics substantially change with the heater configuration and area.[12,46,47] Hence, further research is needed to optimize practical considerations, such as heat source layout and scale.

In this study, we performed pool boiling experiments with a custom multichip module, designed to mimic modern AI multichips packaged with heterogeneous integration. The module has a size of 20 mm × 20 mm and consists of sixteen 3 mm × 3 mm individual heat sources. The resulting heating area is sufficiently large so that the heater size does not affect performance significantly.[44] The pool boiling experiments were performed on smooth surfaces and hierarchical structures, which integrated micropillars on porous copper structures, namely copper inverse opal (CuIO)[48,49] and copper nanowire (NW).[50] We analyzed the composite effects within the hierarchical structures to elucidate the mechanism of CHF and HTC enhancement. Furthermore, in terms of the practical aspects, we visually demonstrated the thermal performance improvements resulting from the synergistic interactions between the multiple heat sources and the hierarchical structures. These insights not only enrich the understanding of enhanced boiling heat transfer mechanisms but also underscore the feasibility and applicability of the proposed thermal management solution.

2. Results and Discussion

We designed and fabricated a multichip module to replicate the thermal load of a modern AI chip (Figure S1, Supporting Information).[12,45] An 8-inch silicon wafer (≈725 μm thick) was cut into 30 mm × 30 mm pieces via die singulation. Then, 16 platinum serpentine thin film heaters, each measuring 3 mm × 3 mm, were fabricated within a 20 mm × 20 mm area on one side of the wafer (Figure S1b, Supporting Information). On the opposite side, we fabricated both smooth surfaces and micropillars with electrodes for subsequent electrodeposition of porous copper structures. The micropillars were created on the silicon wafers through a deep reactive ion etching (DRIE) process. The samples were then cleaved using a wafer-sawing machine and epoxy-bonded to a printed circuit board (PCB) to form the test section (Figure S1a, Supporting Information). Then, we fabricated CuIO and NW-CuIO on the surfaces through electrodeposition and solution immersion, respectively.[49,50] By following a consistent fabrication process, we obtained CuIO with regular pore diameters ($d_p = 1.4\,\mu m$) and neck sizes ($d_n = 0.4\,\mu m$), as determined based on the particle diameter and sintering time of polystyrene (PS), respectively. Further details on these processes are provided in Figure S2 (Supporting Information). **Figure 1** shows scanning electron microscopy (SEM) images of CuIO, NW, and their hierarchical structures integrated into micropillars. Figure 1a,b shows the top and side views of CuIO and NW-CuIO, respectively. These porous copper materials were integrated into micropillars with uniform morphology (Figure 1c), forming

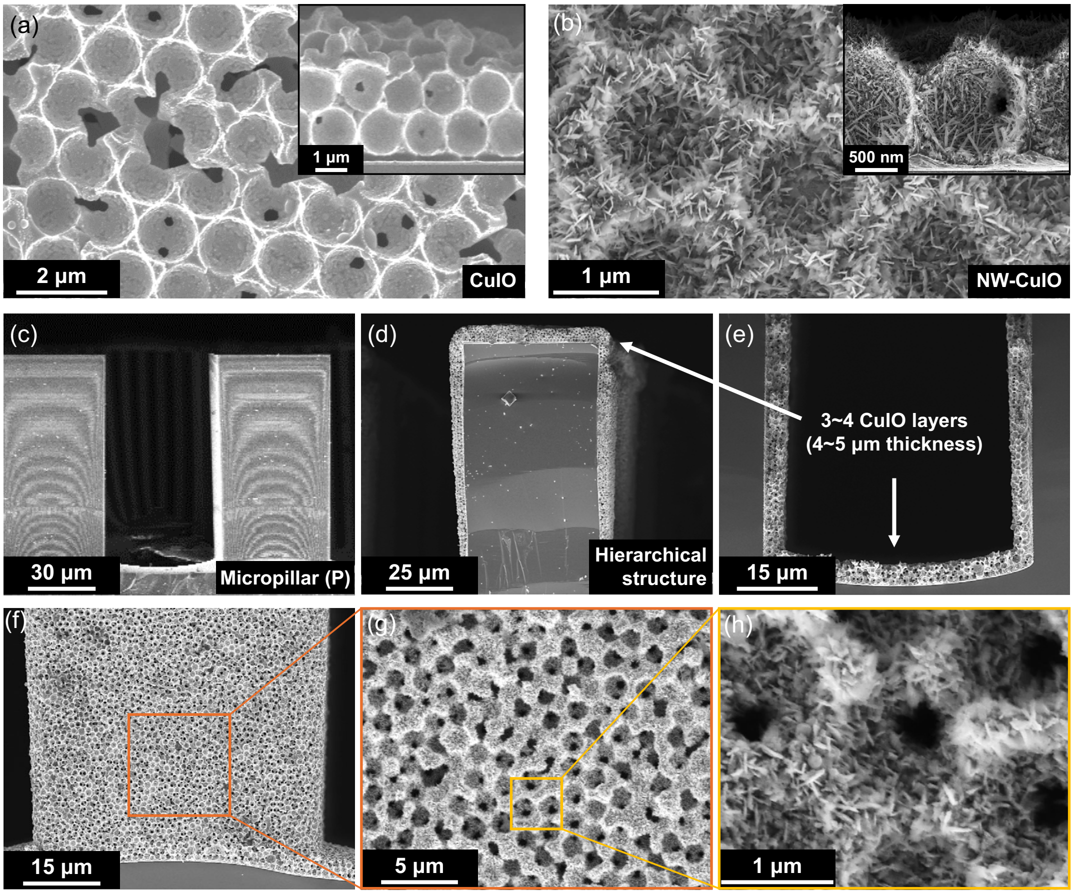

Figure 1. SEM images of CuIO, NW, and their hierarchical structures. a) Top view of CuIO (inset: side view). b) Top view of NW-CuIO (inset: side view). c) Pristine micropillar (P). d,e) Cross-sectional views of CuIO-coated hierarchical structures (P-MH). f–h) Close-up images of NW-CuIO-coated hierarchical structure (P-NH).

hierarchical structures (Figure 1d–h). **Table 1** provides the geometrical information of the fabricated surfaces.

Figure 2a presents the experimentally obtained boiling curves for the smooth surfaces and hierarchical structures. The fabrication of CuIO and NW significantly increased the surface area, improved wettability, and raised the number of nucleation sites, thereby enhancing boiling performance. Specifically, the CHF reached 115 W cm^{-2} on the CuIO smooth surface (S-M) and 141 W cm^{-2} on the NW-CuIO smooth surface (S-N), representing 31 and 60% enhancements, respectively, relative to the CHF of 88 W cm^{-2} on the pristine smooth surface (S). The CHF enhancement was particularly significant in the hierarchical structures combining porous copper with micropillars. The P-NH structure achieved the highest CHF (234 W cm^{-2}), a 166% increase over S. Similarly, P-NH2, with fins that were 50% narrower and spaced closer together, exhibited a CHF of 218 W cm^{-2}. The high CHF of S-N, P-NH, and P-NH2 can be attributed to not only the increased heat transfer area but also the enhanced surface wettability, which facilitate rapid rewetting and delay the occurrence of irreversible dry-out under high-heat flux conditions.[51] When the NW was fabricated on the CuIO to produce NW-CuIO, the hydrophilic surface, having a contact angle of 40°, became structurally more wettable, transforming into a superhydrophilic surface with a contact angle of ≈1°.

Table 1. Geometrical information and structural features of the samples.

Substrate	Sample	Geometrical information	Structural features
Smooth surfaces	S	–	Smooth silicon
	S-M		CuIO
	S-N		NW-CuIO
Micropillars and hierarchical structures	P	Height: 100 μm Width: 50 μm Spacing: 100 μm	Au
	P-MH		CuIO
	P-NH		NW-CuIO
	P2	Height: 100 μm Width: 25 μm Spacing: 50 μm	Au
	P-MH2		CuIO
	P-NH2		NW-CuIO

Figure 2b compares the CHFs of our micropillars and hierarchical structures with those from force-balanced CHF models,[26,27] accounting for the modifications to the surface characteristics by the micro-nano surface structures. The trends in surface roughness and contact angle, such as the progressive

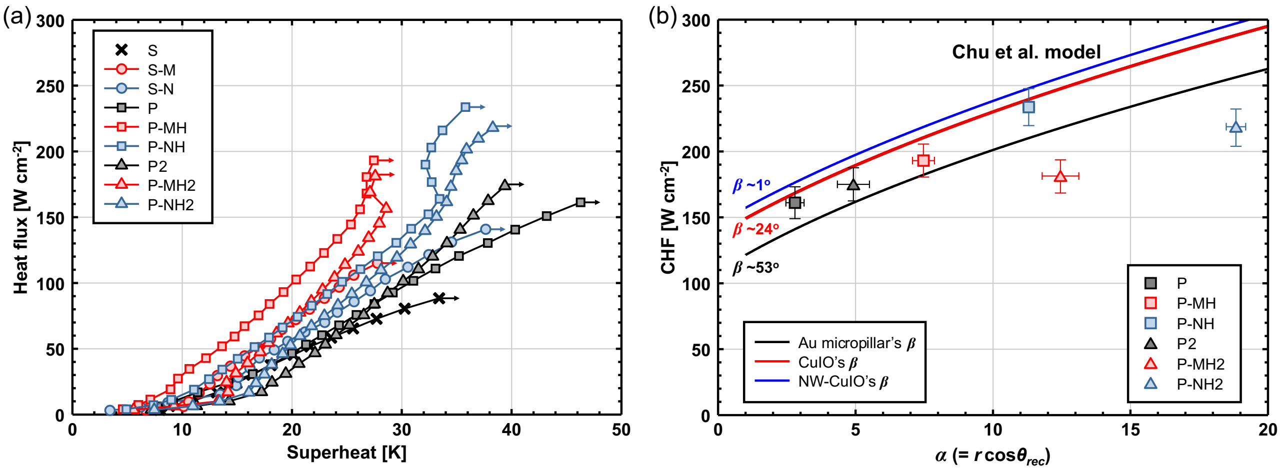

Figure 2. Pool boiling experiment results. a) Heat flux–superheat plot on smooth surfaces of pristine silicon (S), CuIO (S-M), and NW-CuIO (S-N); micropillars (P, P2); and hierarchical structures with micropillars of CuIO (P-MH, P-MH2) and NW-CuIO (P-NH, P-NH2). b) Comparison of CHFs for micropillars and hierarchical structures with force-balanced CHF models. β, r, and θ_{rec} are the apparent receding contact angles, roughness factors, and intrinsic receding contact angles, respectively.

enhancement of CHF with additional surface fabrication, were analytically validated. Further details regarding the contact angle and surface roughness are provided in Figure S3 and Table S1 (Supporting Information). P, P-MH, and P-NH fitted the model well, demonstrating the positive impact of improved surface roughness. However, P-MH2 and P-NH2 did not show corresponding CHF improvement with increasing roughness, deviating from the model. Although P2 achieved a higher CHF than P because of its higher roughness, its high aspect ratio resulted in poor electrodeposition conditions during the subsequent fabrication of CuIO.[52] Consequently, P-MH2 and P-NH2 exhibited relatively poor thermal performance in terms of both CHF and HTC, compared with P-MH and P-NH. The surface SEM images of P2 and P-MH2 are shown in Figure S4 (Supporting Information). The surfaces coated with CuIO exhibited high HTCs (Figure S5, Supporting Information). P-MH achieved the highest HTC (70.3 kW m^{-2} K^{-1}), showing a 166% improvement over S. Similarly, the HTC of P-MH2 was 65.7 kW m^{-2} K^{-1}, which is higher than that of P-NH2. The CuIO-coated structures exhibited higher HTCs than their NW-CuIO-coated counterparts[53] because the microporous surface of CuIO facilitates gas-trapping.[54,55] Unlike NW-CuIO, where most of the cavities are flooded, the circular CuIO layers act as re-entrant cavities and can easily trap gas due to their relatively large contact angle.[40,56–58]

Figure 3 displays high-speed images capturing the dynamics of the bubbles as they depart from the hierarchical surfaces of P-MH and P-NH. Figure 3a,c shows sequential bubble images at low heat fluxes of ≈60 W cm^{-2}. These images indicate that unheated areas can prevent bubble coalescence and continuously provide a liquid supply path. However, the bubble departure behaviors depend highly on the surface conditions when the heat flux is increased. Figure 3b,e shows that the preservation of the liquid supply path is predominantly governed by the departure sizes of the coalescent bubbles. As the high heat flux is applied, the coalescent bubbles grow larger, thereby blocking the liquid supply path, as demonstrated in the Supporting Videos. Once the coalescent bubbles detach, a horizontal liquid supply path can be secured. Note that the departure time of the coalescent bubbles for P-NH (32 ms) is ≈38% shorter than that for P-MH (52 ms) at a high heat flux. This difference indicates that a smaller bubble size and higher departure frequency in P-NH are more conducive to maintaining the liquid supply path at a high heat flux and delaying the CHF. Consequently, P-MH forms larger coalescent bubbles than P-NH, as evident when comparing Figure 3b,d,e. Likewise, the rapid departure of bubbles from the superhydrophilic surface is a natural consequence of its wettability.[59] However, even though the coalescent bubbles are adequately large to have a strong buoyancy force,[60,61] a significant difference in bubble departure time is observed between P-MH and P-NH. This implies that the coalescence dynamics of these large bubbles at high heat fluxes are influenced by factors beyond merely buoyancy and surface wettability. The mechanism behind the dynamics noted in these experiments is difficult to explain fully from observations of only a single or a few coalescent bubbles.

Figure 4a,b shows the bubble coalescence dynamics at high heat fluxes in P-MH and P-NH (same as in Figure 3b,e), respectively, captured over the same time sequence. These images visualize the individual effects of the multiple heaters and fabricated surfaces, along with their synergistic effects on the bubble dynamics. Initially, bubble coalescence occurs only on the scale of a single heater, whereafter the bubbles begin to merge laterally with necking. These coalescent bubbles then spread across the surface, blocking the liquid supply path with a high surface tension force due to the elongated three-phase contact line. At this critical moment, since P-NH is superhydrophilic, the robust liquid inertia force maintains wetting between the heaters and ensures a continuous liquid supply path (second frame in Figure 4b).[62,63] Thus, unlike in P-MH, this liquid supply path prevents the expansion of the three-phase contact line, thereby reducing the surface tension force and promoting bubble

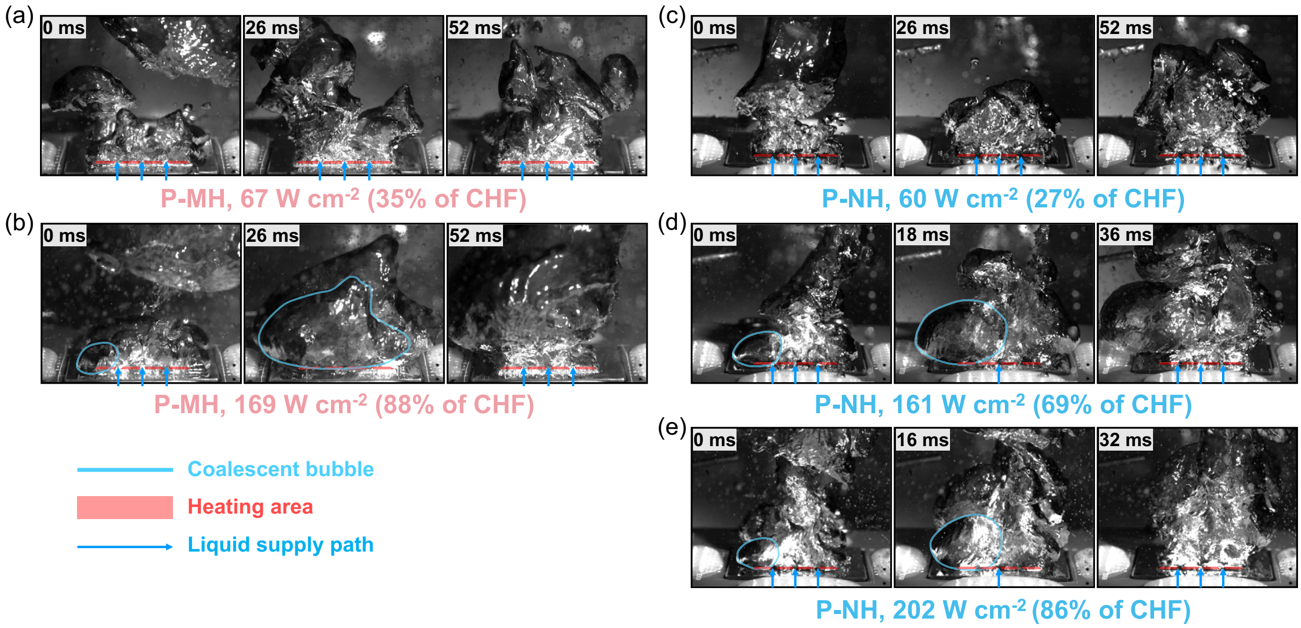

Figure 3. High-speed images captured during pool boiling experiments under different surface conditions, heat fluxes, and sequences. a) Low heat flux in P-MH, b) high heat flux in P-MH, c) low heat flux in P-NH, d) moderate heat flux in P-NH, and e) high heat flux in P-NH.

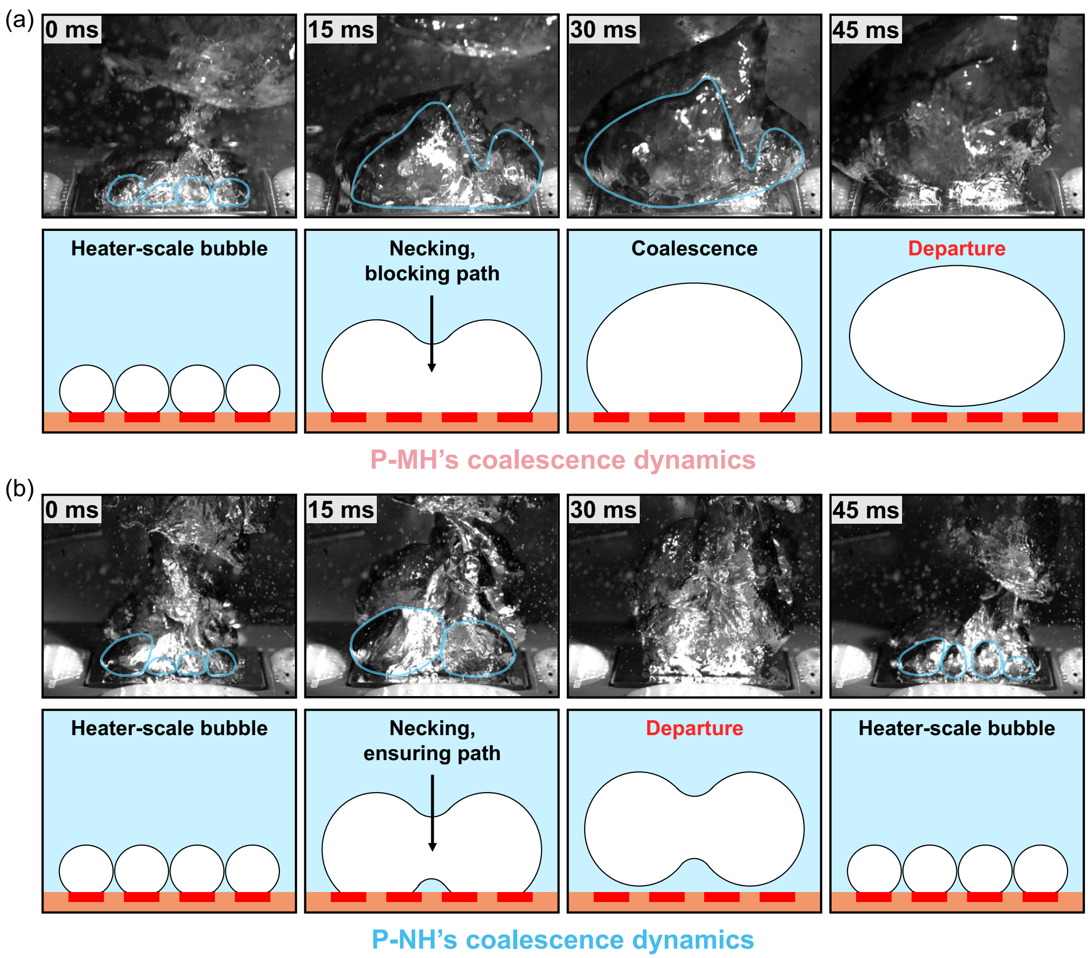

Figure 4. Visualization of bubble coalescence dynamics at high heat flux. High heat fluxes in a) P-MH (88% of CHF) and b) P-NH (86% of CHF).

departure.[29] Consequently, P-NH exhibits much faster bubble coalescence and departure cycles than P-MH.

During pool boiling, a boiling inversion phenomenon is often observed, characterized by the superheat remaining constant or decreasing slightly even in the high heat flux regime. Upon the occurrence of boiling inversion, the HTC improves sharply. Bergles et al.[56] showed that boiling inversion occurs in porous layers, and various hypotheses have been proposed to explain this mechanism.[64–67] Among these, the most convincing explanation is that more nucleation sites are activated at a higher superheat.[36] Hsu's analytical model indicates that with increasing temperature, the minimum diameter of nucleation sites decreases, and more nucleation sites are activated, which has also been confirmed experimentally.[68] This model provides a detailed analytical description of the aforementioned phenomenon, based on which the minimum diameter of the activated nucleation sites is modeled as follows:

$$d_{\min} = \delta\left(\frac{\sin\theta}{1+\cos\theta}\right)\left(1-\sqrt{1-\frac{8\sigma(1+\cos\theta)T_{\text{sat}}}{\rho_g h_{fg}\Delta T_{\text{sat}}\delta}}\right) \tag{1}$$

where δ is the thickness of the thermal boundary layer, while T_{sat}, σ, ρ_g, and h_{fg} denote the saturated temperature, liquid-vapor surface tension, vapor density, and latent heat of water, respectively. Here, θ does not represent only the wettability contact angle; rather, it is the sum of the cavity mouth angle and the wettability contact angle.[69] Due to the difficulty of observing the cavity mouth angle during nucleation, the Hsu model typically assumes this angle to have a specific value, which has been commonly used in subsequent studies.[62] Since the CuIO structures in this study were well-designed with uniform, spherical-shaped cavities, the cavity mouth angle was nearly zero in our experiments.[54] Given that the bubble departure diameter is significantly larger than the pore diameter, we can consider θ to be simply the wettability contact angle.[70] Here, we explain the boiling inversion phenomenon as an increase in the number of activated nucleation sites based on the Hsu model.

Figure 5a shows the HTCs of the micropillars and hierarchical structures as a function of the superheat. The enhancements in HTC occurred at about 27.5 and 33.5 K for the microhierarchical and nanohierarchical structures, respectively. The lack of HTC enhancement in the micropillars suggests that boiling inversion is caused by sequential activation of nucleation sites. Figure 5b shows that the inversion temperatures of the

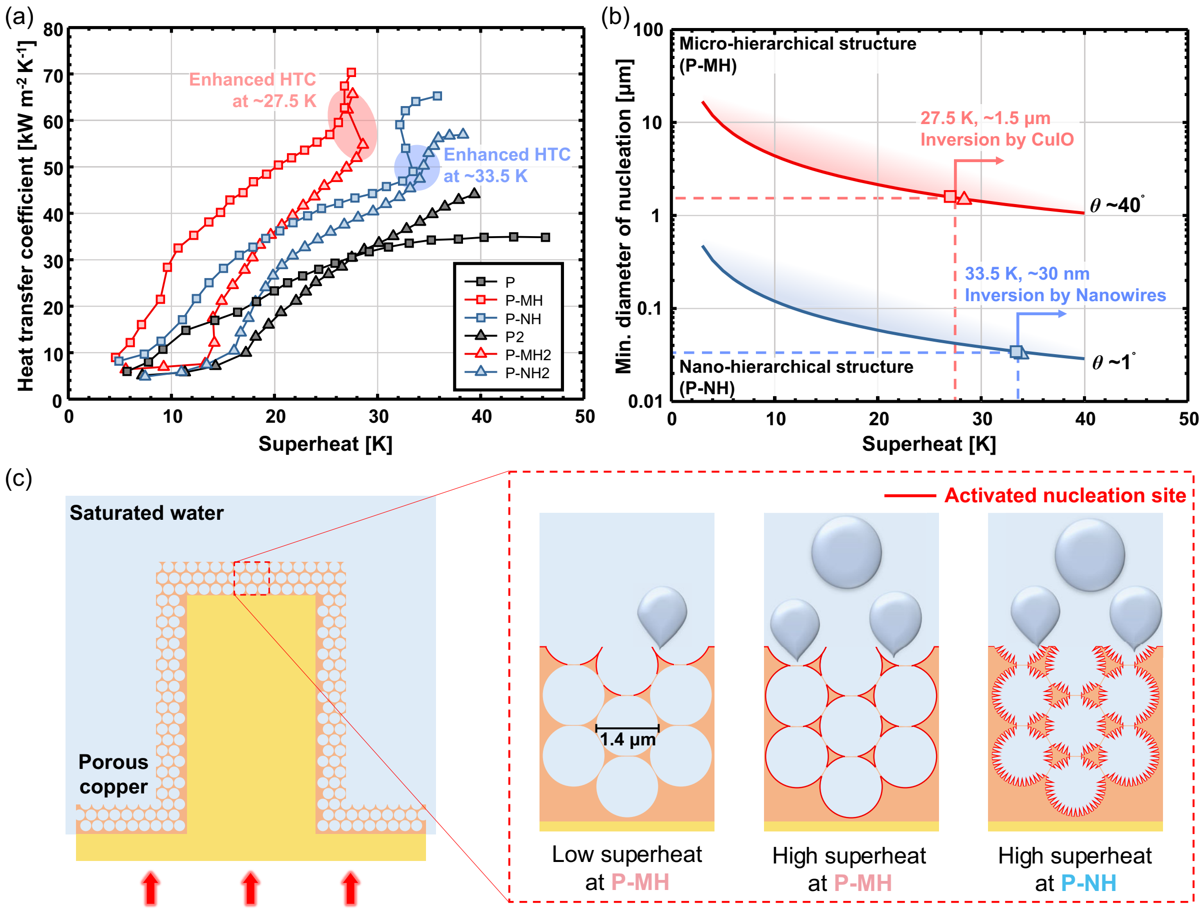

Figure 5. Schematic representation of boiling inversion phenomenon. a) HTC–superheat plots. b) Plot of minimum diameter of activated nucleation site–superheat based on Hsu model considering contact angle of hierarchical structure. c) Schematic illustrating activation of nucleation site by hierarchical structures.

hierarchical structures are consistent with the Hsu model. For the microhierarchical structure with a contact angle of 40°, the superheat leading to boiling inversion was about 27.5 K, at which point the minimum diameter for nucleation site activation was about 1.5 μm. This value is comparable to the d_p of CuIO (≈1.4 μm), which analytically indicates that microscale nucleation sites are secondarily activated by CuIO. Likewise, in the nanohierarchical structure with a contact angle of 1°, boiling inversion occurred at a superheat of ≈33.5 K, at which point the nanoscale nucleation sites became activated. All these trends were observed in P-MH2 and P-NH2, as well as in P-MH and P-NH. This indicates that secondary activation of microscale and nanoscale nucleation sites occurs reliably, regardless of the electrodeposition conditions. Figure 5c schematically describes the nucleation site activation based on the Hsu model. As the superheat increases, the number of activated nucleation sites inside the porous layer increases as well. This leads to more nucleation and HTC enhancement. Since the structural features of the nanohierarchical structure's cavities are difficult to examine, the inversion temperature is also difficult to characterize accurately, as mentioned earlier. Therefore, some studies have reported boiling inversion at relatively low temperatures,[65,71] while others, including this study, have recorded this phenomenon at higher temperatures.[27,28,68] Although more research is required to understand the mechanisms behind the inversion phenomena at high and low temperatures, they yield similar outcomes in that both microscale and nanoscale nucleation sites become activated.

The heating area is one of the parameters affecting pool boiling thermal performance.[44] Its impact becomes pronounced when it is reduced to below 20 × 20 mm, with particularly strong effects observed at around 10 × 10 mm.[72,73] Furthermore, the thermal management approach for an AI chip package with a heterogeneous integration solution differs from that for a conventional chip configuration. Most heat sources are partitioned during the packaging process. Therefore, considering that a 10 × 10 mm die consisting of a single heater is rarely employed in actual applications, utilizing a 20 × 20 mm area for experiments represents a more practical and cost-effective approach. **Figure 6** shows comparison plots of CHF and HTC as functions of the heating area during pool boiling experiments in saturated water with the hierarchical structures fabricated in this study (P-MH, P-NH).[74–76] The corresponding benchmark data are provided in Table S2 (Supporting Information). Among these benchmark studies, most silicon-based experiments with high CHFs were performed on a 10 × 10 mm area,[28,38,68] and a decrease in CHF was observed as the area increased within the same experiment.[44,46] As seen in Figure 6, the benchmarks with higher HTCs appear shifted to the left (squares and hexagons), whereas those with relatively low HTCs appear on the right (circles and triangles). As the heater size increases, CHF and HTC decrease due to the longer liquid supply path; however, structured surfaces can mitigate this problem due to their improved wettability.[46]

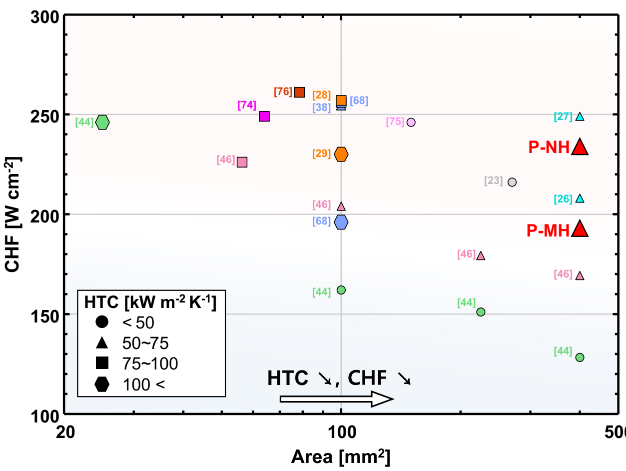

Figure 6. CHF and HTC versus surface area for P-NH and P-MH benchmarked against other studies.

3. Conclusion

In this study, we comprehensively analyzed pool boiling heat transfer using custom multichip modules on 20 × 20 mm surfaces with hierarchical structures. The integration of micropillars with CuIO and NW significantly enhanced both CHF and HTC. The highest CHF, reaching 234 W cm^{-2} in the nanohierarchical structure, was attributed to a delayed dry-out facilitated by enhanced wettability. Furthermore, we visually confirmed that the distinct heater configuration of the multichip is conducive to liquid replenishment, demonstrating a synergistic effect on the superhydrophilic surface. The best HTC, which reached 70.3 kW m^{-2} K^{-1} in the microhierarchical structure, was ascribed to the porous structure's ability to trap gas. A secondary HTC enhancement was also observed in both hierarchical structures, which was consistent with boiling inversion trends related to uniformly engineered porous structures. These findings not only enrich the fundamental understanding of boiling heat transfer over a large-area silicon but also demonstrate the feasibility and effectiveness of hierarchical structures for thermal management in high-performance electronic systems and data centers. Overall, the insights obtained regarding the relationship between surface features, heating layout, and thermal performance provide a valuable framework for developing next-generation cooling technologies.

4. Experimental Section

Fabrication of Multichip Module and Test Section: We performed pool boiling experiments on 20 mm × 20 mm areas of smooth surfaces and micropillars integrated with porous copper (CuIO and NW). To create the smooth surfaces, a 20-nm/500-nm-thick Ti/Pt layer was deposited on the silicon wafer using the sputtering technique. Regarding the micropillars, the DRIE process was first employed to fabricate square micropillars, which included a silicon dry process (Bosch process) to fabricate geometries with a high aspect ratio. Second, 20 nm Ti and 500 nm Au thin films were sputtered onto the micropillars. The Ti layers on each surface functioned as an adhesive layer, and both the Pt and Au thin films served as electrodes for the subsequent porous copper electrodeposition process. On the wafer's bottom surface within a 20 mm × 20 mm area, 16 individual platinum serpentine thin film heaters were designed. The fabricated wafers were bonded to a PCB to form the custom test section. The detailed heater layout is presented in Figure S1 (Supporting Information).

Surface Fabrication Processes for CuIO and NW: The fabrication processes for CuIO and NW are illustrated in Figure S2 (Supporting

Information).[49,50] First, a 5.0% weight/volume PS particle/water suspension was dispensed using the drop-casting method. At this point, the micropillars were exposed to an oxygen plasma for 20 s to enable the PS particles in the dispensed suspension to sediment uniformly. PS particles with a diameter of 1.4 μm ($d_p = 1.4$ μm) were used in this process. The micropillars were then heated to 60 °C to evaporate water and sediment the PS particles in the suspension. Subsequently, the micropillars were sintered in an oven at 98 °C for 30 min to create a neck of about 0.4 μm between the contact surfaces of the PS spheres. Next, pulse electrodeposition was performed at 2.5 mA cm^{-2}, involving alternating one-second-on and one-second-off cycles for 80 min using a potentiostat (BioLogic SP-300). For this process, a 0.4 M $CuSO_4$ + 0.015 M H_2SO_4 aqueous solution, a copper substrate, an Au electrode on the wafer, and an Ag/AgCl reference were used as the electrolyte, anode, cathode, and reference electrode, respectively. After electrodeposition, the wafer was immersed in tetrahydrofuran for 24 h to dissolve the PS template, yielding about 5 μm-thick CuIO-coated microhierarchical structure. The NW was fabricated using a method involving immersion in an aqueous solution. By immersing CuIO in a 0.25 M NaOH + 0.025 M $K_2S_2O_8$ aqueous solution at 60 °C for 10 min, the copper was coated with NW to form NW-CuIO structures. The chemical reaction is as follows:

$$Cu + 2NaOH + K_2S_2O_8 \rightarrow Na_2SO_4 + K_2SO_4 + CuO + H_2O \qquad (2)$$

Pool Boiling Setup and Data Acquisition System: Figure S1c (Supporting Information) schematically illustrates the experimental setup used for the pool boiling tests. The chamber was made of polycarbonate (thermal conductivity = 0.2 W m^{-1} K^{-1}) to minimize heat loss during the experiment. An immersion cartridge heater was installed at the bottom of the chamber to regulate the temperature of the working fluid (deionized water) and to degas the fluid prior to the experiment. The temperature of the bulk liquid was monitored through a K-type thermocouple (±1.0 °C) placed inside the chamber to ensure saturation conditions throughout the experiment. A coil condenser, connected to a loop chiller (JeioTech Co., HH20), was placed at the top of the chamber to condense any vaporized fluid and maintain steady-state conditions. The test section, comprising a wafer bonded to a PCB substrate, was fixed to the chamber's center floor. The 16 individual heaters were connected to corresponding pads on the PCB, with power being supplied via an EX300-12 power source to generate Joule heating. A high-speed camera (Photron FASTCAM Mini UX100) was positioned in front of the chamber to capture the real-time bubble dynamics during the experiment. Images were recorded at 4000 frames per second, and the sequences displayed in Figure 3 and 4 are provided in the Supporting Videos (Supporting Information). The total heat input was measured using a voltage divider circuit composed of two resistors (39 kΩ and 1 kΩ) and a 0.1 Ω ± 1% shunt resistor. After steady-state conditions were reached, the current and voltage data for the platinum thin film heaters were collected using an NI Compact data acquisition (DAQ) system (NI 9220) controlled through the LabVIEW software program. The surface temperature was determined by measuring the resistance changes in each of the 16 heaters. The information regarding a resistance temperature detector calibration for each heater is provided in Figure S6 (Supporting Information). Since the DAQ system measured the temperature at the junction between the PCB and the wafer (i.e., the bottom temperature of the wafer), the surface temperature was calculated via 1-D conduction modeling in MATLAB R2023b. All heat flux and temperature data presented herein were averaged across the 16 heaters. Uncertainties were estimated using the error backpropagation method, as detailed in Section III in the Supporting Information.

Supporting Information

Supporting Information is available from the Wiley Online Library or from the author.

Acknowledgements

This work was supported by the International Cooperative R&D Program of the Korea Institute of Energy Technology Evaluation and Planning (KETEP), a grant funded by the Ministry of Trade, Industry & Energy, Korea (No. RS-2024-00436521), Samsung Advanced Institute of Technology, and the Chung-Ang University Graduate Research Scholarship of 2024.

Conflict of Interest

The authors declare no conflict of interest.

Author Contributions

Youngseob Lee: data curation (lead); formal analysis (lead); investigation (lead); methodology (lead); writing—original draft (lead). **Kiwan Kim**: investigation (supporting); methodology (supporting); writing—original draft (supporting). **Yunseo Kim**: formal analysis (supporting); investigation (supporting); methodology (supporting). **Daeyoung Kong**: formal analysis (supporting); methodology (supporting). **Jeonghwan Park**: data curation (supporting); investigation (supporting). **Daehyuk Son**: project administration (lead); supervision (lead). **Sungchan Kang**: funding acquisition (equal); supervision (equal). **Seogwoo Hong**: project administration (equal); supervision (equal). **Hyoungsoon Lee**: funding acquisition (lead); project administration (lead); supervision (lead); writing—review & editing (lead).

Data Availability Statement

The data that support the findings of this study are available from the corresponding author upon reasonable request.

Keywords

critical heat flux, heat transfer coefficient, hierarchical structures, multichip modules, pool boiling

Received: September 26, 2024
Revised: December 2, 2024
Published online:

[1] Z. Li, H. Luo, Y. Jiang, H. Liu, L. Xu, K. Cao, H. Wu, P. Gao, H. Liu, *Appl. Therm. Eng.* **2024**, *251*, 123612.
[2] N. Jones, *Nature* **2018**, *561*, 163.
[3] Y.-C. Wang, J. Xue, C. Wei, C.-C. J. Kuo, *IEEE Open J. Commun. Soc.* **2023**, *4*, 2952.
[4] C. Stoll, U. Gallersdörfer, L. Klaaßen, *Joule* **2022**, *6*, 2668.
[5] L. Belkhir, A. Elmeligi, *J. Clean. Prod.* **2018**, *177*, 448.
[6] C. Nadjahi, H. Louahlia, S. Lemasson, *Sustain. Comput. Inform. Syst.* **2018**, *19*, 14.
[7] K. M. U. Ahmed, M. H. J. Bollen, M. Alvarez, *IEEE Access* **2021**, *9*, 152536.
[8] R. Zhao, Y. Du, X. Yang, Z. Zhou, W. Wang, X. Yang, *Energy Build.* **2023**, *297*, 113486.
[9] *Energy Efficient Thermal Management of Data Centers* (Eds: Y. Joshi, P. Kumar), Springer US, Boston, MA **2012**.
[10] Q. Zhang, Z. Meng, X. Hong, Y. Zhan, J. Liu, J. Dong, T. Bai, J. Niu, M. J. Deen, *J. Syst. Archit.* **2021**, *119*, 102253.
[11] Y. Sun, N. B. Agostini, S. Dong, D. Kaeli, arXiv, **2020**.

[12] B. Ramakrishnan, S. H. Bhavnani, J. Gess, R. W. Knight, D. Harris, R. W. Johnson, in *The IEEE Semiconductor Thermal Measurement and Management Symp. (SEMI-THERM)*, San Jose, CA USA March **2014**.
[13] Z. He, Y. Yan, Z. Zhang, *Energy* **2021**, *216*, 119223.
[14] A. Habibi Khalaj, S. K. Halgamuge, *Appl. Energy* **2017**, *205*, 1165.
[15] D. Kong, H. Kwon, B. Jang, H.-J. Kwon, M. Asheghi, K. E. Goodson, H. Lee, *Energy Convers. Manag.* **2024**, *315*, 118809.
[16] S. Sarkar, R. Gupta, T. Roy, R. Ganguly, C. M. Megaridis, *Int. J. Heat Mass Transf.* **2023**, *206*, 123888.
[17] R. Kandasamy, J. Y. Ho, P. Liu, T. N. Wong, K. C. Toh, S. J. Chua, *Appl. Energy* **2022**, *305*, 117816.
[18] D. Fan, J. Fang, W. Tong, W. Du, Q. Li, *Cell Rep. Phys. Sci.* **2024**, *1*, 102156.
[19] S. Cho, D. Kong, G. Geum, S. Kang, J. Hyeuk Seo, J. S. Kim, S. H. Lee, J. Lee, H. Lee, *Appl. Therm. Eng.* **2023**, *235*, 121327.
[20] X. Yuan, Y. Du, J. Su, *Renew. Sustain. Energy Rev.* **2022**, *156*, 111974.
[21] G. Liang, I. Mudawar, *Int. J. Heat Mass Transf.* **2019**, *128*, 892.
[22] H. Chu, X. Yu, H. Jiang, D. Wang, N. Xu, *Int. J. Heat Mass Transf.* **2023**, *200*, 123530.
[23] S. H. Kim, G. C. Lee, J. Y. Kang, K. Moriyama, M. H. Kim, H. S. Park, *Int. J. Heat Mass Transf.* **2015**, *91*, 1140.
[24] H. O'Hanley, C. Coyle, J. Buongiorno, T. McKrell, L.-W. Hu, M. Rubner, R. Cohen, *Appl. Phys. Lett.* **2013**, *103*, 024102.
[25] S. G. Kandlikar, *J. Heat Transf.* **2001**, *123*, 1071.
[26] K.-H. Chu, R. Enright, E. N. Wang, *Appl. Phys. Lett.* **2012**, *100*, 241603.
[27] K.-H. Chu, Y. Soo Joung, R. Enright, C. R. Buie, E. N. Wang, *Appl. Phys. Lett.* **2013**, *102*, 151602.
[28] M. M. Rahman, E. Ölçeroğlu, M. McCarthy, *Langmuir* **2014**, *30*, 11225.
[29] M. M. Rahman, J. Pollack, M. McCarthy, *Sci. Rep.* **2015**, *5*, 13145.
[30] A. R. Betz, J. Xu, H. Qiu, D. Attinger, *Appl. Phys. Lett.* **2010**, *97*, 141909.
[31] A. R. Betz, J. Jenkins, C.-J. "CJ" Kim, D. Attinger, *Int. J. Heat Mass Transf.* **2013**, *57*, 733.
[32] D. I. Shim, W.-T. Hsu, M. Yun, D. Lee, B. S. Kim, H. H. Cho, *Int. J. Mech. Sci.* **2023**, *249*, 108280.
[33] Y. Zhang, S. Wang, *Appl. Therm. Eng.* **2022**, *205*, 117925.
[34] A. Fazeli, S. Moghaddam, *Sci. Rep.* **2017**, *7*, 5184.
[35] S. R. Tamvada, S. Moghaddam, *Appl. Therm. Eng.* **2023**, *228*, 120556.
[36] Y. Y. Hsu, *J. Heat Transf.* **1962**, *84*, 207.
[37] P. Griffith, J. D. Wallis, *The Role of Surface Conditions in Nucleate Boiling*, Massachusetts Institute of Technology, Division of Industrial Cooperation, Cambridge, MA **1958**.
[38] Y. Song, S. Gong, G. Vaartstra, E. N. Wang, *ACS Appl. Mater. Interfaces* **2021**, *13*, 12629.
[39] B. Liu, X. Yang, Q. Li, H. Chang, Y. Qiu, *Int. Commun. Heat Mass Transf.* **2022**, *138*, 106350.
[40] C.-J. Kuo, Y. Peles, *Int. J. Heat Mass Transf.* **2007**, *50*, 4513.
[41] H. J. Cho, J. P. Mizerak, E. N. Wang, *Nat. Commun.* **2015**, *6*, 8599.
[42] M. R. Mata, B. Ortiz, D. Luhar, V. Evereux, H. J. Cho, *Sci. Rep.* **2022**, *12*, 18170.
[43] S. Y. Hou, W. C. Chen, C. Hu, C. Chiu, K. C. Ting, T. S. Lin, W. H. Wei, W. C. Chiou, V. J. C. Lin, V. C. Y. Chang, C. T. Wang, C. H. Wu, D. Yu, *IEEE Trans. Electron Devices* **2017**, *64*, 4071.
[44] M.-C. Lu, R. Chen, V. Srinivasan, V. P. Carey, A. Majumdar, *Int. J. Heat Mass Transf.* **2011**, *54*, 5359.
[45] L. Zheng, Y. Zhang, M. S. Bakir, *IEEE Trans. Compon. Packag. Manuf. Technol.* **2015**, *5*, 1379.
[46] S. M. Kwark, M. Amaya, R. Kumar, G. Moreno, S. M. You, *Int. J. Heat Mass Transf.* **2010**, *53*, 5199.
[47] C. Zhang, P. Cheng, F. Hong, *Int. J. Heat Mass Transf.* **2016**, *101*, 1331.
[48] C. Zhang, J. W. Palko, M. T. Barako, M. Asheghi, J. G. Santiago, K. E. Goodson, *Adv. Funct. Mater.* **2018**, *28*, 1803689.
[49] K. Kim, D. Kong, Y. Kim, B. Jang, J. Cho, H.-J. Kwon, H. Lee, *Appl. Therm. Eng.* **2024**, *241*, 122325.
[50] Q. Pan, H. Jin, H. Wang, *Nanotechnology* **2007**, *18*, 355605.
[51] S. J. Kim, I. C. Bang, J. Buongiorno, L. W. Hu, *Int. J. Heat Mass Transf.* **2007**, *50*, 4105.
[52] J. W. Palko, H. Lee, C. Zhang, T. J. Dusseault, T. Maitra, Y. Won, D. D. Agonafer, J. Moss, F. Houshmand, G. Rong, J. D. Wilbur, D. Rockosi, I. Mykyta, D. Resler, D. Altman, M. Asheghi, J. G. Santiago, K. E. Goodson, *Adv. Funct. Mater.* **2017**, *27*, 1703265.
[53] M. M. Rahman, M. McCarthy, *J. Heat Transf.* **2017**, *139*, 111508.
[54] C. H. Wang, V. K. Dhir, *J. Heat Transf.* **1993**, *115*, 670.
[55] C. H. Wang, V. K. Dhir, *J. Heat Transf.* **1993**, *115*, 659.
[56] A. E. Bergles, M. C. Chyu, *J. Heat Transf.* **1982**, *104*, 279.
[57] B. J. Jones, S. V. Garimella, in *ASME/JSME 2007 Thermal Engineering Heat Transfer Summer Conf.*, Vancouver, British Columbia, Canada, July **2007**.
[58] C. H. Li, R. P. Rioux, *Sci. Rep.* **2016**, *6*, 37044.
[59] Y. Nam, E. Aktinol, V. K. Dhir, Y. S. Ju, *Int. J. Heat Mass Transf.* **2011**, *54*, 1572.
[60] R. Iwata, L. Zhang, Z. Lu, S. Gong, J. Du, E. N. Wang, *Langmuir* **2022**, *38*, 4371.
[61] H. Park, S. F. Ahmadi, T. P. Foulkes, J. B. Boreyko, *Adv. Funct. Mater.* **2023**, *34*, 2312088.
[62] R. Chen, M.-C. Lu, V. Srinivasan, Z. Wang, H. H. Cho, A. Majumdar, *Nano Lett.* **2009**, *9*, 548.
[63] H. Bian, C. Kurwitz, Z. Sun, K. Cheng, K. Chen, *Appl. Therm. Eng.* **2018**, *141*, 422.
[64] A. Jaikumar, S. G. Kandlikar, *Appl. Phys. Lett.* **2017**, *110*, 094107.
[65] C. Kruse, A. Tsubaki, C. Zuhlke, T. Anderson, D. Alexander, G. Gogos, S. Ndao, *Appl. Phys. Lett.* **2016**, *108*, 051602.
[66] H. S. Ahn, J. M. Kim, M. Kaviany, M. H. Kim, *Int. J. Heat Mass Transf.* **2014**, *78*, 224.
[67] J. Long, Z. Liu, Z. Cao, J. Wu, X. Xie, *Appl. Therm. Eng.* **2024**, *241*, 122330.
[68] Y. Song, C. D. Díaz-Marín, L. Zhang, H. Cha, Y. Zhao, E. N. Wang, *Adv. Mater.* **2022**, *34*, 2200899.
[69] M. M. Mahmoud, T. G. Karayiannis, *Therm. Sci. Eng. Prog.* **2021**, *25*, 101024.
[70] R. Iwata, L. Zhang, K. L. Wilke, S. Gong, M. He, B. M. Gallant, E. N. Wang, *Joule* **2021**, *5*, 887.
[71] A. Hadžić, M. Može, M. Zupančič, I. Golobič, *Adv. Funct. Mater.* **2024**, *34*, 2310662.
[72] T. G. Theofanous, T. N. Dinh, J. P. Tu, A. T. Dinh, *Exp. Therm. Fluid Sci.* **2002**, *26*, 793.
[73] M. He, Y. Lee, *Therm. Sci. Eng. Prog.* **2019**, *14*, 100421.
[74] R. Wen, Q. Li, W. Wang, B. Latour, C. H. Li, C. Li, Y.-C. Lee, R. Yang, *Nano Energy* **2017**, *38*, 59.
[75] S. Kim, H. D. Kim, H. Kim, H. S. Ahn, H. Jo, J. Kim, M. H. Kim, *Exp. Therm. Fluid Sci.* **2010**, *34*, 487.
[76] B. June Zhang, K. J. Kim, *Appl. Phys. Lett.* **2012**, *101*, 054104.

